

# Chapter 22

## Detection and Tracking of Melt Pool in Blown Powder Deposition Through Image Processing of Infrared Camera Data



Sreekar Karnati and Frank F. Liou

### Abbreviations

AM	Additive manufacturing
BPD	Blown powder deposition
CCD	Charge coupled device
CNC	Computer numerical control
IR	Infra-red
JSR	Just solidified region
LoG	Laplacian of Gaussian

### 22.1 Introduction

Additive Manufacturing (AM) is a component fabrication methodology where the desired geometries are built by selectively adding material in a layer by layer fashion. This approach is complementary to conventional subtractive fabrication methodologies where the desired geometries are machined to shape by removing material from a starting block of material. AM has been theorized to offer cost-effective means to fabricate complex geometries which are otherwise challenging to produce. Through various implementations, AM processes are being developed and commercialized for several materials such as plastics, metals, ceramics, and even organic materials. The avenues offered through AM are often cited to be exciting and groundbreaking.

---

S. Karnati (✉) · F. F. Liou  
Department of Mechanical and Aerospace Engineering, Missouri University of Science and Technology, Rolla, MO, USA  
e-mail: [skw92@mst.edu](mailto:skw92@mst.edu); [liou@mst.edu](mailto:liou@mst.edu)

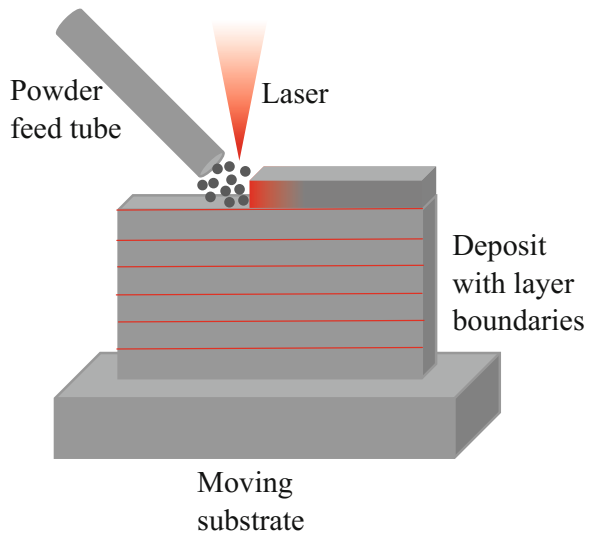
Among the different modalities of AM, metal-based AM is of great interest to the industries such as bio-medical [1], aerospace [2], defense [3], automobile [4], and construction industries [5]. AM is known to provide cost-efficient means of fabricating components with low buy to fly ratios and shorter lead times. The capability of AM to fabricate complex geometries can eliminate the need for assembly and thereby improve manufacturing and functioning efficiencies. AM has also been used to repair, recondition, and remanufacture existing components [6]. Such a revival of the end of life components can lead to immense cost savings and thereby growth in the industry [7].

While the benefits of AM are obvious, the process is very complicated and the outcome from the process is dependent on various factors. Depending on the modality, the factors of influence are subject to change. Metal-based AM modalities differ in terms of power source, the form of feedstock, types of process variables, and capabilities [8]. For the sake of clarity and brevity, discussion in this chapter will be limited to blown powder deposition.

Blown Powder Deposition (BPD) is a variant of laser metal deposition [8]. In this process, a moving melt pool is created on a substrate material by the use of a laser and a motorized worktable. A stream of powder is introduced into the melt pool through a feed tube; this powder is melted and then consolidated on to the substrate material. By moving the melt pool in a pre-planned fashion, the material is deposited in a layer by layer sequence. Upon successful deposition of such layers, the components of required geometries are fabricated. A schematic diagram of BPD is shown in Fig. 22.1.

The quality and properties of components obtained through BPD are dependent on process variables such as laser power, scan speed, powder feed, and layer thickness [9–11]. Creating and sustaining a melt pool capable of producing material with

**Fig. 22.1** A schematic diagram of a front view of a BPD process indicating the relative positions of the laser beam, the powder feed tube, and the substrate. The red lines indicate the layer boundaries from the preplanned deposition path



required properties while ensuring successful fabrication of the required geometry is a challenging problem [12]. In the aim of understanding the influence of process parameters on material properties, researchers have mostly relied on experimentation and subsequent testing [10]. The composition of the material under discussion also influences the interaction and influence of the process parameters. This forces researchers to repeat similar studies on every new material.

Analysis from destructive testing of deposits only yields information on the final outcome and leaves in-process phenomenon to speculation. In order to realize the in-process phenomenon, researchers have often resorted to numerical analysis such as finite element modeling [13], cellular automaton [14], molecular dynamics [15], and phase field modeling [16]. Researchers have used such techniques to model, cooling rate [17], melt pool characteristics [18], temperature profile microstructure [19, 20], residual stresses [21], etc. In order to establish the validity of these models, the attributes of deposits such as melt pool dimensions, microstructure features, residual strain, and the temperature during deposition have been used. While such approaches have known to be successful, wide-scale incorporation of these models is not feasible. Often times these studies are limited in their scope due to assumptions necessary to facilitate successful calculation, loss of relevancy due to change in setup or limitations on computational resources.

Vision-based real-time monitoring of the deposition processes and closed loop control is a potential solution for realizing in-process phenomenon and performing a controlled deposition process. Real-time monitoring and potential closed-loop control of AM processes have been a topic of study for a while. Song et al. have successfully developed a system of three CCD cameras and a pyrometer for real-time tracking and control of deposition height. While doing so they were also able to measure and control the melt pool temperature [22]. The required control actions were performed by manipulating the power value during deposition. Similar process monitoring techniques have been developed for another localized heating process, i.e., welding. Real-time monitoring and correction during plasma welding and laser welding were achieved to study weld pool diameter, the surface of the weld pool, the weld plume size, etc. Kovacevic et al. utilized a CCD camera to capture a laser illuminated weld pool for information on surface detail. By its study, they were able to perform real-time correction during the process [23]. This camera was configured to capture light in the wavelength range of the irradiating laser. Manipulation of arc current, shield gas flow rate, and feed speed were used as a means to perform the required control. Zhang et al. utilized a spectrometer to analyze the plasma-developed laser lap welding. Simultaneously, a CCD camera was used to co-axially monitor the shape of the weld pool [24]. The intensity of characteristic peaks pertaining to constituent elements was observed to understand the welding practice. By integrating image processing and edge detection methods, they identified potential defects during the process. Huang et al. utilized an IR camera to acquire temperature information and implement interference analysis on their hybrid laser and TIG welding system. By doing so, they were successful in tracking the weld seam during the process [25]. Similarly, multiple systems were developed using pyrometers, CCD cameras, acoustic sensors, etc. to monitor the process [26–29]. The above-

mentioned control and monitoring setups were dedicated to observing a characteristic feature such as the size of melt or weld pool, temperature, the shape of weld plume, etc. Decision criteria based on this information were established through iterative experimentation. However, the analysis did not involve decoupling the monitored data to understand the solidification process. These setups were validated through qualification of final geometry. In this chapter though, a processing methodology for obtaining representative insight into the process of solidification is discussed. The influence and capacity of feedback systems are presented.

## 22.2 Influence of Feedback Systems

The authors theorize, controlling and maintaining a fixed melt pool size and ensuring consistent material deposition is central to setting up a robust deposition process. Incorporation of feedback mechanisms for compensating in-process inconsistencies and ensuring consistent layer thickness could be an approach for reliable fabrication. Pan and his colleagues at Missouri S&T developed a BPD system with two feedback systems aimed at managing the energy within the deposit and ensuring consistent material buildup [30].

Due to the localized heating in BPD, there are steep temperature gradients within and around the melt pool. Also, due to the large melting points of most metals, the melt pool is visibly hot and distinguishable. This enables the prospect of incorporating vision-based process monitoring systems based on cameras, both visible and infrared. Such cameras are excellent choices for gathering spatial and thermal information. However, these cameras yield large amounts of data. Feedback systems based on camera data are often slow due to the computational overhead originating from the need for massive data processing. For a fast and dynamic process such as BPD, incorporating camera-based feedback systems is still a challenging problem. However, vision-based sensing is still viable with analog high-speed sensors such as photodiodes and pyrometers. Due to the low-resolution aspect of these sensors, decoupling complex concurrent phenomenon can be challenging. There is a need for capturing such sensor data under various known conditions to establish process signatures.

In this section, the fabrication of AISI 316 stainless steel thin wall structures using BPD under the influence of two closed-loop feedback systems is discussed. Stainless powder in the particle size range of  $-100/+325$  mesh was used to perform the deposition. A 1 kW fiber laser with a wavelength of 1064 nm was used in combination with a CNC worktable to perform these depositions. The CNC deposition system involved the use of stepper motors to achieve actuation. The process of micro-stepping was used to achieve smooth motion during deposition.

A FLIR A615 thermal infrared camera was used to monitor the deposition process. The A615 is a longwave infrared camera, which involves the use of micro-bolometers as the sensors. It is sensitive to infrared light in the spectrum range of 7.5–13.5  $\mu\text{m}$ . The camera has a maximum resolution of  $640 \times 480$  pixels. Under the calibrated

conditions, the camera is capable of sensing temperature up to a resolution of 50 mK. The lens used for the current set of analyses had a field of view of 25°. The camera was capable of reaching a frame rate of 200 frames per second.

Pan's feedback systems were used during these depositions. These systems can be classified as an energy management system and a height control system. These systems have been proven to successfully fabricate thin wall structures that met the design requirements [30]. Incorporation of these control systems facilitated near constant bead thickness, reliable material build, and good surface quality. Deposits fabricated with and without the influence of these control systems are shown in Fig. 22.2. The deposit fabricated under the influence of the control systems is visually better and has more consistent geometric features. The surface roughness was also better when fabricating under the influence of the control systems. The logic and setup of these control systems are discussed in sections below.

### 22.2.1 Energy Management System

From Planck's law, the spectral radiance of a black body at a constant temperature can be analytically modeled. The spectral radiance of a black body at a given wavelength can be calculated from Eq. (22.1).

$$B_{\lambda}(\lambda, T) = \frac{2hc^2}{\lambda^5} \frac{1}{e^{\frac{hc}{\lambda k_B T}} - 1} \quad (22.1)$$



**Fig. 22.2** Thin wall deposits fabricated without (left) and with (right) the control of feedback systems

Where,  $B_{\lambda}(\lambda, T)$  is the spectral radiance observed at a wavelength  $\lambda$ ,  $T$  is the absolute temperature of the blackbody,  $k_B$  is the Boltzmann constant,  $h$  is the Plank's constant, and  $c$  is the speed of light in the medium. From Wein's law, the peak of the spectral radiance curve occurs at wavelengths that is inversely proportional to the temperature of the black body. From these laws, it can be inferred that for a fixed shape and fixed thermal gradient the total spectral radiance in a given spectral range should be fixed. The energy management system monitors and attempts to control this radiance. This control is expected to indirectly correlate with the melt pool. In order to maintain the required radiance value, the system manipulates the input power during deposition. In case the measured radiance value is high, the control system drives the power down and vice versa. The logic flow of the energy management system is shown in Fig. 22.3.

While the radiance of the deposition site was monitored, the significance of the numerical value was not analyzed as a part of this study and setup. There is merit in understanding the contribution of each source, i.e., molten material and the just solidified material. However, this requires a more specialized investigation which goes beyond the scope of this work. For the current study, the optimized setting for

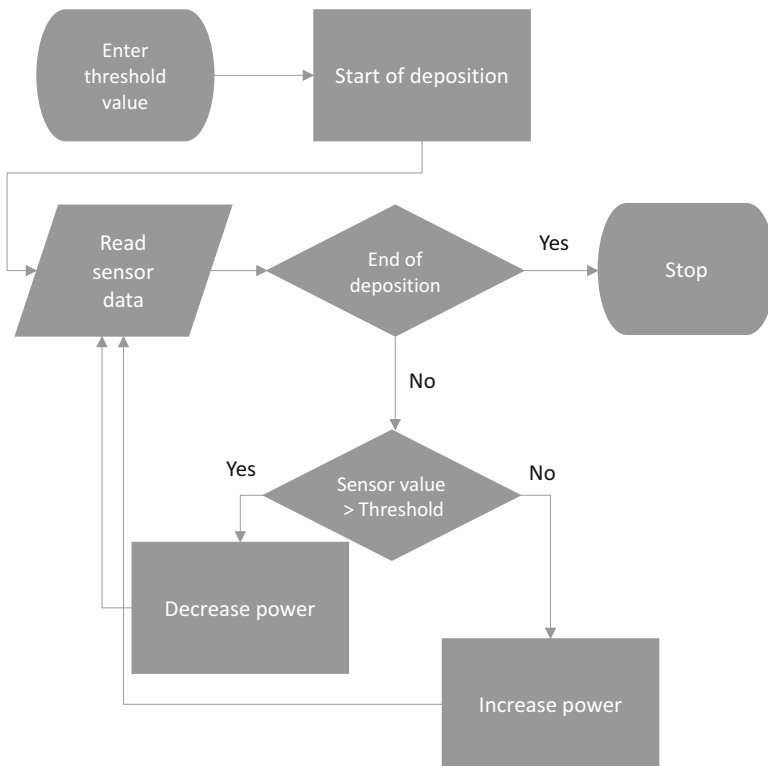


Fig. 22.3 Flowchart detailing the workflow of the energy management system

the energy management system was evaluated experimentally through trial and error. The optimal condition was chosen based on the size of the high temperature region during deposition. The outcome material quality was also inspected to ensure good bonding between successive layers and no porosity.

### **22.2.2 Height Control System**

For the purposes of distance measurement, triangulation methods are often used in industrial environments using automation and vision-based sensing [31, 32]. The process typically involves lasers and light sensors to calculate the distance between two points. Extensions of this implementation have been used to even create 2D and 3D topographic profiles. There is a benefit to using such implementations in additive manufacturing. Monitoring build height enables reliable part fabrication and in-process correction [33, 34]. A similar implementation was used in the current setup as well. Instead of a laser-based setup, a temperature sensor based setup was used for triangulation.

The height control system is used to monitor and control the building height during BPD. The feedback system employs a non-contact temperature sensor to keep track of the top of the deposit. This sensor was a dual color pyrometer procured from WilliamsonIR. The camera was capable of measuring temperatures above 900 °C. Due to the dual color implementation, the pyrometer can bypass the issues of emissivity variance. The system uses a temperature threshold to assess the material buildup. The system employs a go/no go strategy to ensure the required build height during deposition. The control system manipulates the motion system to go forward when the intended buildup is attained and slows down or stops motion when the material buildup is below the requirement. These decisions are taken along the entire deposition tool path. A flowchart detailing the workflow of the height control system is shown in Fig. 22.4.

The energy management system and the height control system work in conjunction to facilitate reliable deposition during BPD. One of the biggest issues in BPD that leads to problems during deposition is capture efficiency. In order to maintain consistent layer thickness, the capture efficiency of the melt pool has to remain constant. In case the efficiency is more than nominal, the material buildup will be larger than the layer thickness. If the efficiency is lower than nominal, the buildup will be lower than the layer thickness. The pileup of these differences will lead to unsuccessful deposition. Under the right conditions, when the capture efficiency is close to nominal and the right power, feed rate, and scan speed are set, the deposition reaches a steady state and doesn't need any intervention.

Typically, the right deposition conditions are evaluated using a lengthy and expensive design of experiments study. However, in this case, the energy management system and the height control system can be used to tune the machine settings and obtain the right deposition parameters. While identifying a domain of viable parameters settings is made easy, picking the best setting by visually inspecting the

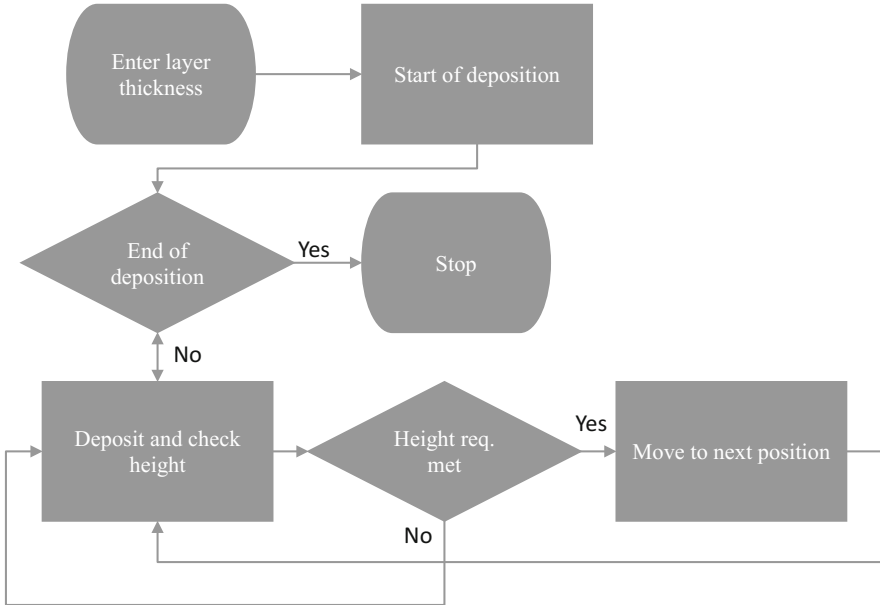


**Fig. 22.4** Flowchart detailing the workflow of the height control system

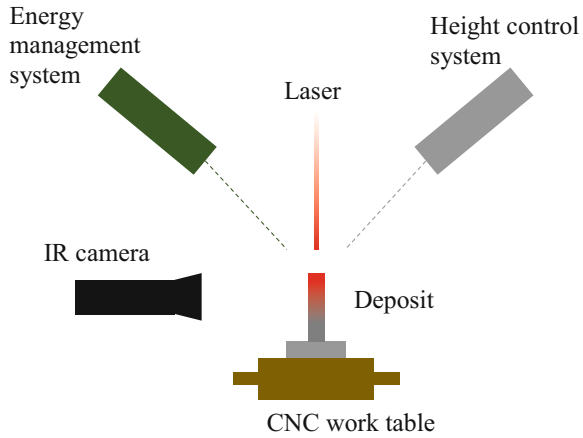
deposit quality is not optimal. The complex interaction of the energy management system and height control system could lead to largely varying thermal conditions which could lead to inhomogeneity in material properties [10, 35, 36]. While many factors influence the material properties, thermal history can be considered as one of the most influential factors. Using thermal cameras to capture and analyze thermal history during deposition could serve as an evaluation tool to pick the appropriate process parameters.

A schematic drawing of the deposition setup is shown in Fig. 22.5. The IR camera was oriented normal to the deposit in order to capture the deposition process from a front view perspective. In this orientation, the camera is capable of recording a longitudinal view of the active region during deposition. The IR thermography is a surface measurement technique and does not provide insight into the variation of these measurements along the thickness of the deposit. The temperature gradients beneath the surface cannot be measured using this technique.

The variation in the total area of the high temperature region was used as a metric to assess the influence and difference with varying control system parameters. The high temperature region was defined as the region whose radiance is above a threshold value. The chosen threshold was set to the value corresponding to a temperature of  $50^\circ$  lower than the solidus temperature of 316 stainless steel. This was supposed to imply that the area on the deposit meeting the threshold criteria would constitute the material that had just solidified. However, that is not the case. The above equations and discussions pertaining to radiance are limited to that of a black body. In reality,



**Fig. 22.5** Schematic side view diagram illustrating the setup of the feedback systems on the BPD system



most materials do not behave like a black body. Their radiance at a given temperature is a partial fraction of that of a black body at a similar temperature. These bodies are referred to as grey bodies. The radiative powder ( $W$ ) from a grey body at a temperature ( $T$ ) with a surrounding temperature ( $T_c$ ) can be defined as Eq. (22.2). This equation, the Stefan–Boltzmann Law, is obtained by integrating the Plank’s law for all wavelengths. Emissivity ( $\epsilon$ ) is used to account for the lower radiation values of grey bodies. The value of the emissivity for grey bodies falls between 0 and 1. The “ $\sigma$ ” is the Stefan–Boltzmann constant.

$$W = \epsilon \sigma A \left( T^4 - T_c^4 \right) \tag{22.2}$$

The infrared cameras measure the radiative power given off a grey or black body. Under the right setup conditions and setup calibration, these power values can be processed and interpreted as temperatures. Multiple sources contribute to the total radiative power value measured by the IR camera ( $W_{\text{camera}}$ ). The breakdown of different sources contributing to the total radiative power measured by the IR camera is shown in Fig. 22.6. The body of interest, hot body, is shown in red. The temperature of the hot body is  $T_{\text{HB}}$ . The emissivity of the hot body is  $\epsilon$ . The black body radiative power from the hot body is  $W_{\text{HB}}$ . The reflected temperature is  $T_{\text{RT}}$  and the radiative component is  $W_{\text{RT}}$ . The atmospheric temperature is  $T_{\text{atm}}$  and the radiative power component is  $W_{\text{atm}}$ . The transmissivity of the atmosphere is  $\tau$ . The makeup of the total radiative power as measured by the IR camera is expressed as Eq. (22.3). The emissivity and transmissivity values are used to decouple the radiative power values measured by the camera. The decoupled power components are used to estimate the absolute temperature values.

$$W_{\text{camera}} = \epsilon \tau W_{\text{HB}} + (1 - \epsilon) \tau W_{\text{RT}} + (1 - \tau) W_{\text{atm}} \tag{22.3}$$

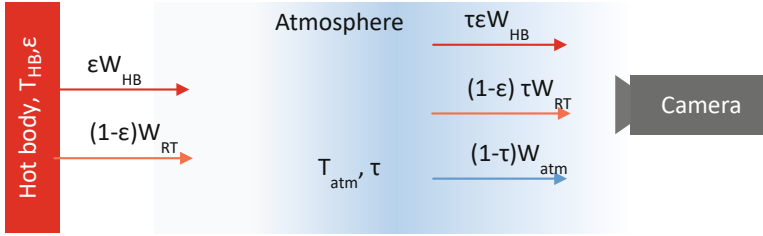


**Fig. 22.6** Illustration demonstrating the breakdown of the total radiative powder measured by the IR camera

These power measurements are also influenced by the setup conditions and are sensitive to the range of temperature under study. The calibration of the camera and measurement setup is therefore essential for obtaining true temperature measurements. The complexity and sensitivity of the calibration and setup process make it challenging to obtain true temperature values. However, these challenges are minimized when used for purposes of differential thermography. The analysis discussed in this chapter involves the use of differential thermography and not absolute temperature measurement. A calibrated setup is doable in cases where the range of measured temperatures is small and the emissivity values are also known. However, the emissivity values for a given material are subject to change with temperature, wavelength, and phase change. Typically, the emissivity of metal drops when a phase change happens from solid to liquid state. This is attributed to the rise in reflectivity of the molten material. The same is true for the case of 316 stainless steel. In the case of BPD, the range of temperatures seen is very large and the process also involves phase change. Adding to this complexity, depending on the setup, the region of interest can be moving with the field of view. By the definition set for the high temperature region in the above paragraphs of discussion, this region could include portions or all of the melt pool. Further discussion on the constitution of the high temperature region will be continued in the next sections of the chapter.

### 22.2.3 Variation in the High Temperature Region

The deposition of 25 mm  $\times$  25 mm 316 stainless steel thin wall structures under the control of feedback systems for different powder feed settings was monitored using the IR camera. For a fixed threshold value on the energy management system and layer thickness, the deposition was performed at three different powder feed settings. A powder feed rate of 10, 30, and 50 gm/min was used for deposition. Argon gas was used to shield the deposition from oxidation.

A snapshot of the BPD process during the fabrication of a thin wall 316 stainless steel structure is shown in Fig. 22.7. This was generated using a false color rendering to realize the variation in temperature, where purple indicates the lower end of the

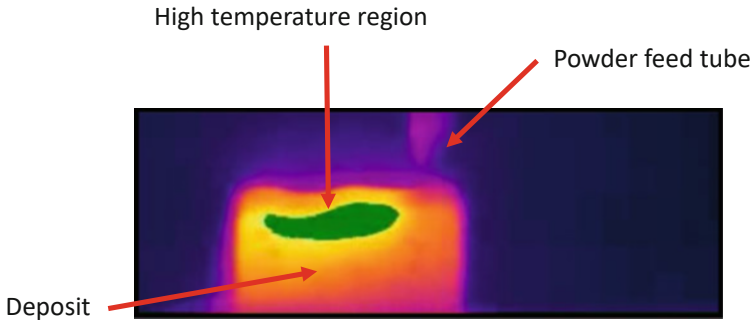


**Fig. 22.7** Infrared thermograph of BPD of 316 stainless steel captured from a front view perspective. The green color represents the high temperature region

data and yellow indicates the higher end of the data. The deposit and powder feed tube can be seen within the picture. The thermal data was processed to identify the pixels that met the threshold criteria for the high temperature region. The pixels corresponding to the high temperature region are highlighted in green as shown in Fig. 22.7.

During deposition, the height control system checks to ensure sufficient material buildup. In case the required level was not reached, the control system slows down or stops the movement. By doing so, the material deposition is continued in the same location and when the required material buildup is attained the deposition system moves on to the next position along the tool path. In situations where the worktable is slowed down or stopped, continuous heating by the laser in the same location leads to heat retention. This can lead to slower cooling rates and in extension weaker material. These issues are supposed to be eliminated through the intervention of the energy management system. In cases of heat buildup, the energy management system lowers the power of the laser and attempts to mitigate heat retention. While this is the expected outcome from the control systems, the final outcome needs to be investigated. Typically destructive testing is employed to draw estimations of cooling rate and heat retention during deposition. However, with the IR camera incorporation, the size of a high temperature region can be monitored to more reliably visualize and optimize the deposition process. The evolution of the size of the high temperature region for each of the powder feed settings can be seen in Fig. 22.8.

From Fig. 22.8, there is a definite variation in the total area of the high temperature region with varying powder feed rate. At the lowest powder feed rate of 10 gm/min, the overall trend in the area of the high temperature region was found to be increasing. However, as the powder feed rate was increased, say for 30 gm/min, the overall value of the high temperature region was substantially reduced. However, steep rises and drops similar to those seen in the case of 10 gm/min still persisted. Upon further increasing powder feed rate to 50 gm/min, the overall area value stayed more consistent and the rises/drops in the values were also reduced. Among the considered

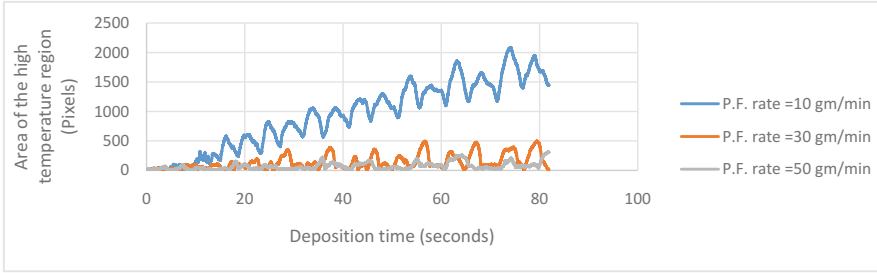


**Fig. 22.8** Variation in the total area of the high temperature region during BPD with varying powder feed (P.F.) rate

powder feed rates, 50 gm/min yielded the most consistent values for the area of the high temperature region.

The overall rise in the area of the high temperature region for the 10 gm/min feed rate was suspected to be the intervention of the height control system. Due to the lower powder feed rate, meeting the requirements for material buildup would be slower in the case of 10 gm/min when compared to 30 and 50 gm/min feed rates. This implies that when the height control system slows down the deposition, there is a rise in heat retention. While the energy management system does lower the power, its intervention is insufficient in avoiding the overall increase in the area of the high temperature region. With the increase in powder feed rate to 30 gm/min, the intervention of the height control system seems to have been reduced and this is reflected in the total area data. However, the energy management system is still not entirely successful in eliminating issues of heat retention. This suggests at this powder feed value, the issue could be from cumulative error. The control system is suspected to be unable to sense minute differences in the material buildup. These differences can stack up over layers and warrant intervention from the height control system. In that instance, while there is a rise in the total area of the high temperature region, the intervention of the energy management system is successful in bringing down the overall value. The power feed rate of 50 gm/min appears to be near optimal. The control systems managed to keep the area of the high temperature region near consistent. Therefore, the optimal powder feed setting among the three settings was concluded to be 50 gm/min.

While deposits made at all the powder feed settings met the required geometric criteria, without the IR camera monitoring, the influence of the control systems would have been challenging to analyze. The analysis of the area of the high temperature region led to valuable insights into the process. However, further dissection of the thermal data is possible. The variation of the emissivity values caused by phase change can help break down the thermal data into the just solidified region and melt pool region.

### 22.3 Melt Pool Identification

The emissivity of the solid 316 stainless is higher than the emissivity of the liquid phase [23, 37]. Also, the emissivity of 316 stainless with an oxidized surface is higher than that of one with a shiny metallic finish. Therefore, from Eq. (22.3), at solidus temperature, the radiation from the melt pool in BPD will be lower than the radiation from the solid metal. If the pixels corresponding to solid and liquid weren't identified and the appropriate emissivity values were not assigned, the temperature measurements from the IR camera can be misleading. For example, if the emissivity for the entire field of view in Fig. 22.7 was set to 0.95, the pixels corresponding to the melt pool would appear colder than the material at solidus temperature. While this, in reality, is not true, this phenomenon can be leveraged to identify the pixels constituting the melt pool.

In an image, a sharp difference in contrast stemming from differences in details is referred to as an edge. By employing edge detection techniques, the pixels in the IR image corresponding to the melt pool could be identified. Since 316 stainless steel is not a eutectic composition, it has a freezing range. Over this range of temperatures, the material gradually transitions from solid to liquid and it is referred to as mushy zone. In BPD, a vague boundary can be seen between the completely liquid phase and the completely solid phase. However, due to the low magnification and resolution of the IR camera ( $640 \times 120$ ) in the current setup, resolving this fuzzy boundary is not expected to be feasible. Therefore, a step-like transition from solid to liquid and vice versa is expected. Due to this lack of distinction between melt pool and mushy zone, from here on the melt pool and the mushy zone are collectively referred to as the melt pool.

$$e_{\text{Just solidified region}} > e_{\text{Melt pool+mushy zone}} > e_{\text{Ambient region}} \quad (22.4)$$

$$W_{\text{Just solidified region}} > W_{\text{Melt pool+mushy zone}} > W_{\text{Ambient region}} \quad (22.5)$$

Figure 22.9 shows a schematic representation of the boundaries formed during deposition and the comparison of the emissivity values. Boundaries in Fig. 22.9 indicate the edges that are possible due to the emissivity differences. Due to the variation in emissivity values, the effective radiative power values and thereby the calculated temperature values also vary and follow the same trend. The effective radiative power is the power value as measured by the camera. The descending order of emissivity and radiative power values are shown in Eqs. (22.4) and (22.5). Through edge detection, these characteristic regions such as the Just Solidified Region (JSR) and the melt pool can be identified. The presence of these differences can be realized by performing a discrete thermal gradient analysis across the horizontal and vertical directions of the thermograph. The peaks observed in these gradients were expected to bear correlation with the transitions in the material's emissivity

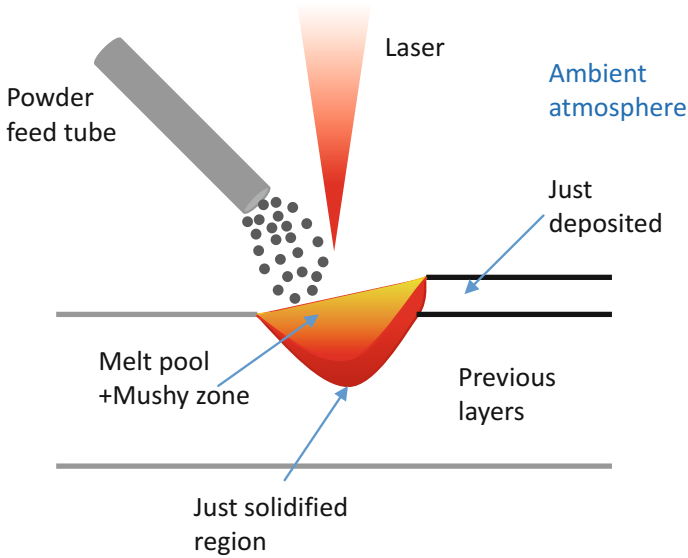


**Fig. 22.9** An illustration of boundaries between different regions of interest and corresponding differences in emissivity

values. The evaluated vertical and horizontal gradients of temperatures (Fig. 22.7) during deposition are shown in Figs. 22.10 and 22.11. The equations used to calculate the discrete gradient are Eqs. (22.6) and (22.7).  $x_{i,j}$  represents the pixel value in the  $(i, j)$  positions of an image.

$$\text{Discrete gradient in } y = x_{i,j} - x_{i,j-1} \quad (22.6)$$

$$\text{Discrete gradient in } x = x_{i,j} - x_{i-1,j} \quad (22.7)$$

Figure 22.10 indicates peaks in the discrete vertical gradient of thermal data from Fig. 22.7; these peaks are expected to represent the vertical transition from the ambient region to deposit. Peaks around the melt pool can also be noticed. Figure 22.11 depicts the discrete horizontal gradient of the thermal data from Fig. 22.7. The peaks in this plot are expected to show the horizontal transitions from the ambient region to deposit and vice versa. The transitions around the melt pool can also be seen in this gradient plot. Laplace edge detection technique was used to isolate the location of these transitions in the deposit. Standard functions from python libraries were implemented to identify these edges. The foreseen edges were captured after a series of smoothing, gradient and edge detection operations. The detailed implementation of processing is presented below.

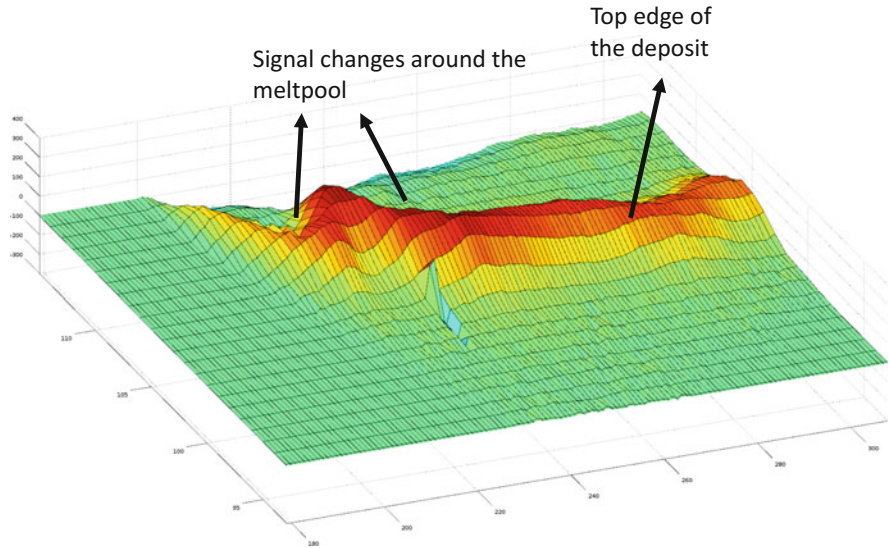


**Fig. 22.10** Peaks occurring around the melt pool and the top edge of the deposit in the surface plot of the discrete gradient of the thermal data along the vertical direction

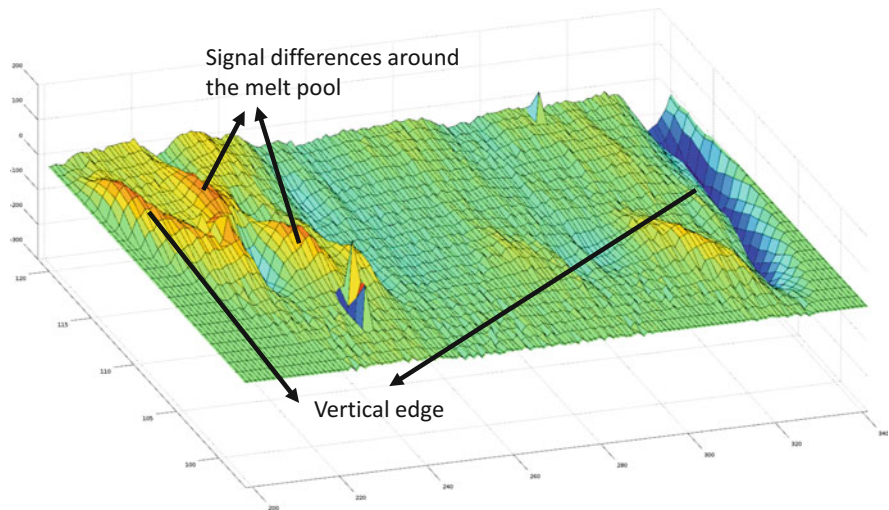


**Fig. 22.11** Peaks occurring around the melt pool and the top edge of the deposit in the surface plot of the discrete gradient of the thermal data along the horizontal direction

### 1. Moving median

Figure 22.12 shows a false color rendering of the output generated after applying a moving median filter. The iron color palette was chosen for rendering, where black is the lowest value and white is the highest value. The moving median was performed by picking the median values among every five consecutive frames. The moving median operation was expected to remove powder particles, oxidation flashes, and Johnson noise. Equation (22.8) details the moving median operation. The  $x_{i,j,t}$  is the pixel value at the  $(i, j)$  position in an image acquired at time  $t$ .  $mx_{i,j,t}$  is the median value gathered across pixels in the same position across five consecutive time steps. This median data was used for further processing.

$$mx_{i,j,t} = \text{Median}(x_{i,j,t-5}, x_{i,j,t}) \quad (22.8)$$

### 2. Gaussian blur and Laplacian transform

A function to perform the Gaussian blur and the Laplace transform (see Eq. (22.9)) was implemented on data outputted in the previous step. The Gaussian blur minimizes spatial noise across the pixels of the image. This operation is necessary since the second derivative operations are very sensitive to noise. Typically these operations are implemented through convolution operations with pre-calculated kernels. The output image is shown in Fig. 22.13. This data from here on is referred to as LoG (Laplacian of Gaussian).

A more localized search was then performed by limiting the search domain to the region inside the deposit boundary. A search for edges with a lower threshold yielded the melt pool boundary solidified region. The processed image with melt pool (red), just solidified region (yellow), and the deposit boundary (blue) shown in Fig. 22.15.

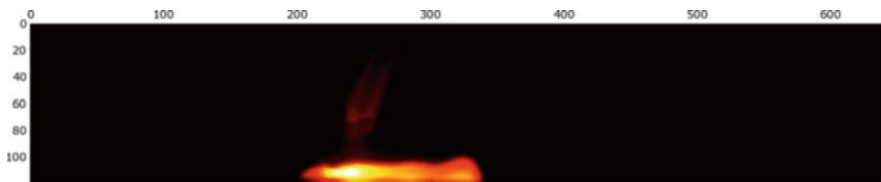


Fig. 22.12 False color image post moving median operation

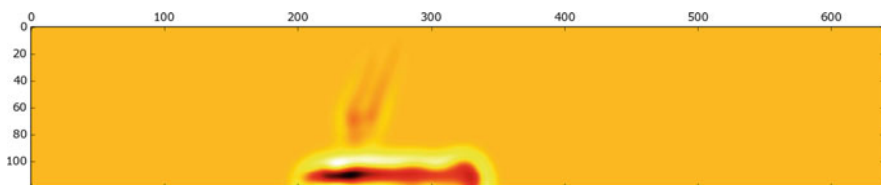


Fig. 22.13 Spatial variation in double discrete deviate of the thermal data from Fig. 22.12



$$L(x, y) = \frac{\partial^2 I(x, y)}{\partial x^2} + \frac{\partial^2 I(x, y)}{\partial y^2} \quad (22.9)$$

### 3. Edge detection

The LoG data was analyzed for identifying edges, and an appropriate threshold value was set to eliminate noise and capture only the most significant changes. The presence of an edge is realized as a zero crossing in the LoG data. A change in sign across consecutive pixels was used to identify these zero crossings. The edges that were identified are shown as a binary image (see Fig. 22.14). The site of an edge was set as 1 and the rest were set to zero. The identified boundaries were found to be those of the deposit and the powder feed tube. While the deposit boundaries were easily identified, the melt pool boundaries were not captured. The transitions corresponding to the melt pool boundary were not substantial enough to meet the set threshold. Thereby the melt pool boundary was not captured at this stage.

Implementing the above steps of image processing led to the generation of data which are visualized in Fig. 22.16 for better understanding. Figure 22.16 shows the first layer of the deposition before the steady state was obtained. As discussed in the previous section, the variation in the just solidified region is substantial before steady state was achieved. This expected due to the intervention of the control systems. Figure 22.17 show snapshots from during deposition after steady state was achieved. The size of the melt pool and the just solidified region remained almost constant post steady state.

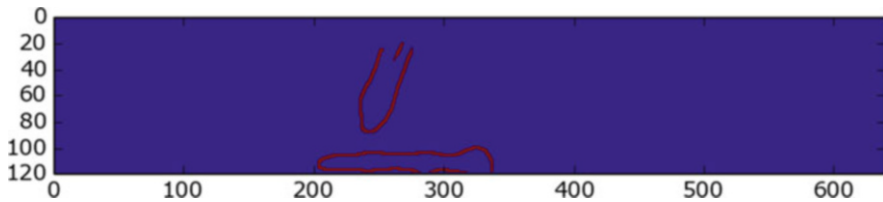


**Fig. 22.14** The edges of the deposit and powder feed tube (red)

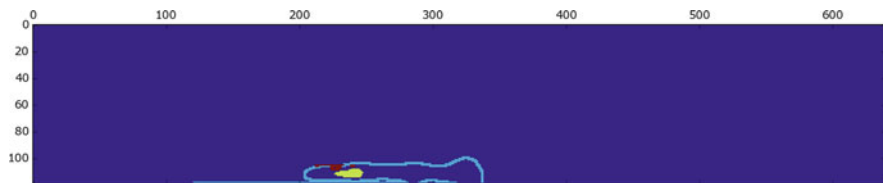


**Fig. 22.15** The melt pool (red) and just solidified region (yellow) boundary of the deposit (sky blue)

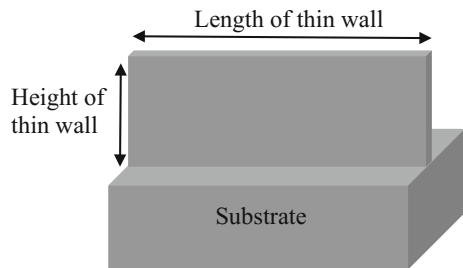


**Fig. 22.16** The first layer of deposition, melt pool (white), just solidified region (yellow), and deposit boundary (red), left to right progression in the deposition



**Fig. 22.17** Melt pool (white), just solidified region (yellow), and deposit boundary (red) after a steady state was achieved by the control system, left to right progression of deposition

**Fig. 22.18** Illustration of thin wall substrates used for line scan depositions



### 22.3.1 Sensitivity and Repeatability

In order to assess the sensitivity of this technique, depositions on substrates machined to the shape of thin wall structures were analyzed. These substrates were machined to have different lengths and heights of the thin wall structure. The shape of these thin wall substrates is defined in Fig. 22.18. These experiments involved four layers of an end to end deposition on each of the substrates. These depositions were monitored using the IR camera to capture the thermal history. To simplify the complexity of the process, these depositions were carried out without the control of the feedback systems.

The analysis of IR data from these deposits indicated a definite impact of substrate length and thin wall height. This influence was theorized to be a consequence of different degrees of heat retention. The difference in heat retention was attributed to the difference in the size of these thin walls and the resulting differences in conduction losses. Larger sizes of high temperature regions were seen on substrates with a smaller length. Due to the small track length, heat retention was observed to be prominent. On the other hand, the deposits with low thin wall heights showed very small sizes of melt pool and just solidified region. The close proximity of the melt pool to the substrate due to the small height of the thin wall leads to low levels of heat retention and in extension small sizes of melt pool and just solidified regions. The analysis of thermal data from deposits on substrates with taller thin walls was also in agreement with this conclusion. Due to the large thin wall heights and distance from

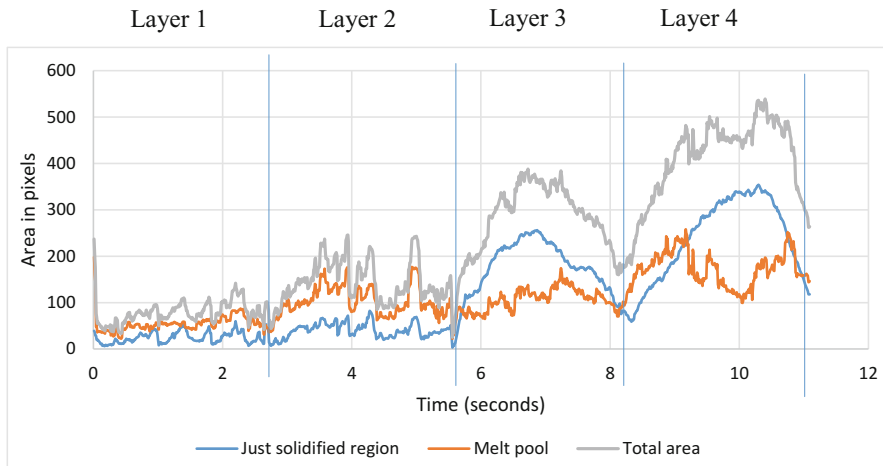


**Fig. 22.19** Variation in areas of just solidified regions and melt pool on a thin wall substrate

the substrate, the heat retention was observed to be significant. Consequently, the total area of the melt pool and just solidified region were observed to be substantially higher. These subtle differences in sizes of melt pool were registered and identified using this monitoring methodology. Analysis of replications of these depositions yielded similar conclusions reliably [38].

The rise and drops in the total area of the high temperature region seen in Fig. 22.8 were attributed to the rise in heat retention. These fluctuations are suspected to be the consequences of thin wall geometry. At the edges of the thin wall, the total area of the melt pool was observed to increase. This phenomenon was observed to be more prominent with increasing heat retention. At the edges, due to the localized heating of BPD, an increase in the size of the melt pool resulted in a corresponding decrease in the size of the just solidified region. However, the overall high temperature region was seen to increase. Previously, this observation was not apparent from only monitoring the high temperature region from the temperature data. Identification of melt pool data is necessary to understand the complete picture during BPD. The variation in the area of the regions of interest is shown in Fig. 22.19.

## 22.4 Conclusions

Acquisition of thermal history through an IR camera was identified to be a viable method for monitoring blown powder deposition process. A methodology was laid out for qualitative analysis of the thermographic data acquired from the IR camera. Monitoring the total area of the material meeting a temperature based criterion was found to be instrumental in assessing the influence of closed loop feedback systems.

An image processing methodology based on edge detection was developed to analyze the IR data. The difference in emissivity values of the solid and liquid phases of metal resulted in sharp changes in the IR data. Edge detection techniques were used to successfully identify these phase transitions. Identification of these transitions led to successful identification of the melt pool.

**Acknowledgments** The financial support from National Science Foundation Grant # CMMI-1625736 and the Intelligent Systems Center (ISC) at Missouri S&T is appreciated.

## References

1. Murr, L. E., Gaytan, S. M., Medina, F., et al. (2010). Next-generation biomedical implants using additive manufacturing of complex, cellular and functional mesh arrays. *Philosophical Transactions. Series A, Mathematical, Physical, and Engineering Sciences*, 368, 1999–2032. <https://doi.org/10.1098/rsta.2010.0010>.
2. Vishnu Prashant Reddy, K., Meera Mirzana, I., & Koti Reddy, A. (2018). Application of additive manufacturing technology to an aerospace component for better trade-off's. *Materials Today: Proceedings*, 5, 3895–3902. <https://doi.org/10.1016/J.MATPR.2017.11.644>.
3. Busachi, A., Erkoyuncu, J., Colegrove, P., et al. (2017). A review of additive manufacturing technology and cost estimation techniques for the defence sector. *CIRP Journal of Manufacturing Science and Technology*, 19, 117–128. <https://doi.org/10.1016/J.CIRPJ.2017.07.001>.
4. Kumar Dama, K., Kumar Malyala, S., Suresh Babu, V., et al. (2017). Development of automotive FlexBody chassis structure in conceptual design phase using additive manufacturing. *Materials Today: Proceedings*, 4, 9919–9923. <https://doi.org/10.1016/J.MATPR.2017.06.294>.
5. Delgado Camacho, D., Clayton, P., O'Brien, W. J., et al. (2018). Applications of additive manufacturing in the construction industry—A forward-looking review. *Automation in Construction*, 89, 110–119. <https://doi.org/10.1016/J.AUTCON.2017.12.031>.
6. Oter, Z. C., Coskun, M., Akca, Y., et al. (2019). Benefits of laser beam based additive manufacturing in die production. *Optik (Stuttgart)*, 176, 175–184. <https://doi.org/10.1016/J.IJLEO.2018.09.079>.
7. Ford, S., & Despeisse, M. (2016). Additive manufacturing and sustainability: An exploratory study of the advantages and challenges. *Journal of Cleaner Production*, 137, 1573–1587. <https://doi.org/10.1016/J.JCLEPRO.2016.04.150>.
8. (10AD) Standard Terminology for Additive Manufacturing Technologies BT—Standard Terminology for Additive Manufacturing Technologies.
9. Lewis, G. K., & Schlienger, E. (2000). Practical considerations and capabilities for laser assisted direct metal deposition. *Materials and Design*, 21, 417–423. [https://doi.org/10.1016/S0261-3069\(99\)00078-3](https://doi.org/10.1016/S0261-3069(99)00078-3).
10. Shamsaei, N., Yadollahi, A., Bian, L., & Thompson, S. M. (2015). An overview of direct laser deposition for additive manufacturing; Part II: Mechanical behavior, process parameter optimization and control. *Additive Manufacturing*, 8, 12–35. <https://doi.org/10.1016/j.addma.2015.07.002>.
11. Dinda, G. P., Dasgupta, A. K., & Mazumder, J. (2009). Laser aided direct metal deposition of Inconel 625 superalloy: Microstructural evolution and thermal stability. *Materials Science and Engineering A*, 509, 98–104. <https://doi.org/10.1016/J.MSEA.2009.01.009>.
12. Mazumder, J., Dutta, D., Kikuchi, N., & Ghosh, A. (2000). Closed loop direct metal deposition: Art to part. *Optics and Lasers in Engineering*, 34, 397–414. [https://doi.org/10.1016/S0143-8166\(00\)00072-5](https://doi.org/10.1016/S0143-8166(00)00072-5).

13. Peyre, P., Aubry, P., Fabbro, R., et al. (2008). Analytical and numerical modelling of the direct metal deposition laser process. *Journal of Physics D: Applied Physics*, *41*, 025403. <https://doi.org/10.1088/0022-3727/41/2/025403>.
14. Javaid, M., & Haleem, A. (2017). Additive manufacturing applications in medical cases: A literature based review. *Alexandria Journal of Medicine*, *54*(4), 411–422. <https://doi.org/10.1016/J.AJME.2017.09.003>.
15. Wang, Y., Wei, Q., Pan, F., et al. (2014). Molecular dynamics simulations for the examination of mechanical properties of hydroxyapatite/poly  $\alpha$ -n-butyl cyanoacrylate under additive manufacturing. *Bio-medical Materials and Engineering*, *24*, 825–833. <https://doi.org/10.3233/BME-130874>.
16. Sahoo, S., & Chou, K. (2016). Phase-field simulation of microstructure evolution of Ti–6Al–4V in electron beam additive manufacturing process. *Additive Manufacturing*, *9*, 14–24. <https://doi.org/10.1016/J.ADDMA.2015.12.005>.
17. Amine, T., Newkirk, J. W., & Liou, F. (2014). An investigation of the effect of direct metal deposition parameters on the characteristics of the deposited layers. *Case Studies in Thermal Engineering*, *3*, 21–34. <https://doi.org/10.1016/J.CSITE.2014.02.002>.
18. Qi, H., Mazumder, J., & Ki, H. (2006). Numerical simulation of heat transfer and fluid flow in coaxial laser cladding process for direct metal deposition. *Journal of Applied Physics*, *100*, 024903. <https://doi.org/10.1063/1.2209807>.
19. Zheng, B., Zhou, Y., Smugeresky, J. E., et al. (2008). Thermal behavior and microstructure evolution during laser deposition with laser-engineered net shaping: Part II. Experimental investigation and discussion. *Metallurgical and Materials Transactions A: Physical Metallurgy and Materials Science*, *39*, 2237–2245. <https://doi.org/10.1007/s11661-008-9566-6>.
20. Zheng, B., Zhou, Y., Smugeresky, J. E., et al. (2008). Thermal behavior and microstructural evolution during laser deposition with laser-engineered net shaping: Part I. Numerical calculations. *Metallurgical and Materials Transactions A: Physical Metallurgy and Materials Science*, *39*, 2228–2236. <https://doi.org/10.1007/s11661-008-9557-7>.
21. Mazumder, J., Choi, J., Nagarathnam, K., et al. (1997). The direct metal deposition of H13 tool steel for 3-D components. *JOM*, *49*, 55–60. <https://doi.org/10.1007/BF02914687>.
22. Song, L., Bagavath-Singh, V., Dutta, B., & Mazumder, J. (2012). Control of melt pool temperature and deposition height during direct metal deposition process. *International Journal of Advanced Manufacturing Technology*, *58*, 247–256. <https://doi.org/10.1007/s00170-011-3395-2>.
23. Kovacevic, R., & Zhang, Y. M. (1997). Real-time image processing for monitoring of free weld pool surface. *Journal of Manufacturing Science and Engineering*, *119*, 161. <https://doi.org/10.1115/1.2831091>.
24. Zhang, Y., Zhang, C., Tan, L., & Li, S. (2013). Coaxial monitoring of the fibre laser lap welding of Zn-coated steel sheets using an auxiliary illuminant. *Optics and Laser Technology*, *50*, 167–175. <https://doi.org/10.1016/j.optlastec.2013.03.001>.
25. Huang, R.-S., Liu, L.-M., & Song, G. (2007). Infrared temperature measurement and interference analysis of magnesium alloys in hybrid laser-TIG welding process. *Materials Science and Engineering A*, *447*, 239–243. <https://doi.org/10.1016/J.MSEA.2006.10.069>.
26. Li, L. (2002). A comparative study of ultrasound emission characteristics in laser processing. *Applied Surface Science*, *186*, 604–610.
27. Gao, J., Qin, G., Yang, J., et al. (2011). Image processing of weld pool and keyhole in Nd:YAG laser welding of stainless steel based on visual sensing. *Transactions of the Nonferrous Metals Society of China*, *21*, 423–428. [https://doi.org/10.1016/S1003-6326\(11\)60731-0](https://doi.org/10.1016/S1003-6326(11)60731-0).
28. Saeed, G., & Zhang, Y. M. (2007). Weld pool surface depth measurement using a calibrated camera and structured light. *Measurement Science and Technology*, *18*, 2570–2578. <https://doi.org/10.1088/0957-0233/18/8/033>.
29. Luo, M., & Shin, Y. C. (2015). Vision-based weld pool boundary extraction and width measurement during keyhole fiber laser welding. *Optics and Lasers in Engineering*, *64*, 59–70. <https://doi.org/10.1016/J.OPTLASENG.2014.07.004>.

30. Pan, Y. (2013). *Part height control of laser metal additive manufacturing process*. Missouri University of Science and Technology.
31. Garcia-Cruz, X. M., Sergiyenko, O. Y., Tyrsa, V., et al. (2014). Optimization of 3D laser scanning speed by use of combined variable step. *Optics and Lasers in Engineering*, *54*, 141–151. <https://doi.org/10.1016/J.OPTLASENG.2013.08.011>.
32. Lindner, L., Sergiyenko, O., Rodríguez-Quíñonez, J. C., et al. (2016). Mobile robot vision system using continuous laser scanning for industrial application. *Industrial Robot: An International Journal*, *43*, 360–369. <https://doi.org/10.1108/IR-01-2016-0048>.
33. Donadello, S., Motta, M., Demir, A. G., & Previtali, B. (2018). Coaxial laser triangulation for height monitoring in laser metal deposition. *Procedia CIRP*, *74*, 144–148. <https://doi.org/10.1016/J.PROCIR.2018.08.066>.
34. Donadello, S., Motta, M., Demir, A. G., & Previtali, B. (2019). Monitoring of laser metal deposition height by means of coaxial laser triangulation. *Optics and Lasers in Engineering*, *112*, 136–144. <https://doi.org/10.1016/J.OPTLASENG.2018.09.012>.
35. Lewandowski, J. J., & Seifi, M. (2016). Metal additive manufacturing: A review of mechanical properties. *Annual Review of Materials Research*, *46*, 151–186. <https://doi.org/10.1146/annurev-matsci-070115-032024>.
36. Carroll, B. E., Palmer, T. A., & Beese, A. M. (2015). Anisotropic tensile behavior of Ti–6Al–4V components fabricated with directed energy deposition additive manufacturing. *Acta Materialia*, *87*, 309–320. <https://doi.org/10.1016/J.ACTAMAT.2014.12.054>.
37. Roger, C. R., Yen, S. H., & Ramanathan, K. G. (1979). Temperature variation of total hemispherical emissivity of stainless steel AISI 304. *Journal of the Optical Society of America*, *69*, 1384. <https://doi.org/10.1364/JOSA.69.001384>.
38. Karnati, S. (2015). *Thermographic investigation of laser metal deposition*. Missouri University of Science and Technology.